Near-surface S-wave velocities estimated from traffic-induced Love waves using seismic interferometry with double beamforming

Nori Nakata[1]

Abstract

I use ambient noise, especially traffic noise, to estimate the 2D near-surface S-velocity distribution. Near-surface velocities are useful for understanding structure, stiffness, porosity, and pore pressure for engineering/environmental purposes and static correction of active-source imaging. I extract Love waves propagating between each receiver pair from 12 h of traffic noise using seismic interferometry with power-normalized cross-correlation. The receiver array contained three parallel lines, each of which had 100 transverse-component geophones. I apply double beamforming to the correlations at the parallel lines for improving the signal-to-noise ratio of the extracted Love waves to satisfy the stationary phase assumption for seismic interferometry. I use these Love waves for a dispersion analysis to estimate a 2D near-surface S-wave velocity model based on the multichannel analysis of surface waves. To improve the lateral resolution of the velocity model, I sort the extracted waves according to common midpoints (CMPs) and limited the maximum offset of receiver pairs. The dispersion analysis at each CMP is based on the assumption of layered media, and using all CMPs, I can estimate high-resolution 2D velocities down to 80 m depth. The velocity variations are similar to the location of strong reflectors obtained by a previous study. The main features of the velocity model are recovered even from 1 h of continuous traffic-noise data, which means that the proposed technique can be used for efficient 4D surveys.

Introduction

Knowledge of the near-surface velocity structure is important for geophysical engineering, environmental geophysics, hydrogeology, mining, and static correction for active-seismic imaging. Boreholes and logging tools are useful for understanding the near surface, but they are expensive and have almost no lateral sensitivity. Surface-wave analyses are alternatives to examine the near-surface properties (Socco et al., 2010). The dispersive characteristic of surface waves relates to the spatial variation of the subsurface velocities, especially for S-waves (Gabriels et al., 1987). Multichannel analysis of surface waves (MASW) can improve the estimation of dispersion curves and avoid spatial aliasing (Park et al., 1999). Hayashi and Suzuki (2004) use a concept of common mid point (CMP) for MASW to enhance the lateral resolution, and Ikeda et al. (2013) further improve the lateral resolution by changing the maximum offsets of the CMP gathers for each frequency. We can apply MASW to active and passive seismic source data (Park et al., 2007), and here, I retrieve pseudoactive data by applying seismic interferometry to ambient noise (particularly traffic noise) and then use CMP-based MASW to estimate 2D near-surface S-wave velocities.

Seismic interferometry is a correlation-based process to retrieve coherent wave propagation between receivers from chaotic wavefields, and these retrieved waves are useful for imaging earth's subsurface. Theoretically, we can apply this method to surface and body waves in various frequencies (Aki, 1957; Claerbout, 1968; Lobkis and Weaver, 2001; Wapenaar, 2004). Practically, wave types and frequency ranges for ambient-noise seismic interferometry are controlled by the excitation of ambient seismic fields and the structure of wave paths. Because one can observe strong seismic waves around the frequency band of second microseisms (5–8 s) everywhere in the world (Peterson, 1993), applications of ambient-noise seismic interferometry for imaging mostly focus on the crustal-global scale (Shapiro et al., 2005; Nishida et al., 2009). When receiver arrays are close to the oceanic coast or other noise sources (e.g., active volcanoes), we can retrieve high-frequency signals and use them for imaging (Brenguier et al., 2007; Young et al., 2011). Traffic-induced seismic waves also contain high-frequency energy, and thus, one can use them for near-surface characterization (Nakata et al., 2011; Behm et al., 2014). If the receiver spacing is small, we have more chances to extract high-frequency signals because we can reduce

[1]Stanford University, Stanford, California, USA and University of Oklahoma, Norman, Oklahoma, USA. E-mail: nnakata@stanford.edu; nnakata@ou.edu.

Manuscript received by the Editor 21 January 2016; revised manuscript received 18 April 2016; published online 4 August 2016. This paper appears in *Interpretation*, Vol. 4, No. 4 (November 2016); p. SQ23–SQ31, 11 FIGS.

http://dx.doi.org/10.1190/INT-2016-0013.1.

spatial aliasing (Lin et al., 2013; Mordret et al., 2013). Although body-wave retrieval from ambient fields is difficult because the dominant wave types in ambient fields are surface waves (Ekström, 2001), Nakata et al. (2015) extract P-waves by using a dense receiver array and estimated 3D velocities.

To retrieve Green's function between receivers from ambient fields, stationary phases have the largest contribution (Snieder, 2004). Strong nonstationary phases often lessen the signal-to-noise-ratio (S/N) of the retrieved wavefields, which might lead to misinterpretation of wave types and/or structure. I use double-beamforming (DBF) techniques for enhancing the stationary-phase contribution while suppressing other waves. The DBF is one of the array-based signal processing techniques to identify wave types and/or isolate particular waves based on the slowness and azimuth of the waves (Rost and Thomas, 2002; Roux et al., 2008). Boué et al. (2014) use DBF to improve the accuracy of tomograms inverted from surface waves recorded by USArray. Nakata et al. (2016) extract direct and reflected surface and body waves by noise correlation with DBF at Piton de la Fournaise Volcano, France.

In this study, I estimate near-surface S-wave velocities from traffic-induced seismic wavefields. First, I introduce the observed data, and then extract Love waves by using seismic interferometry and DBF. Then, I apply CMP-based dispersion analyses to estimate the 2D S-wave velocities with high lateral resolution.

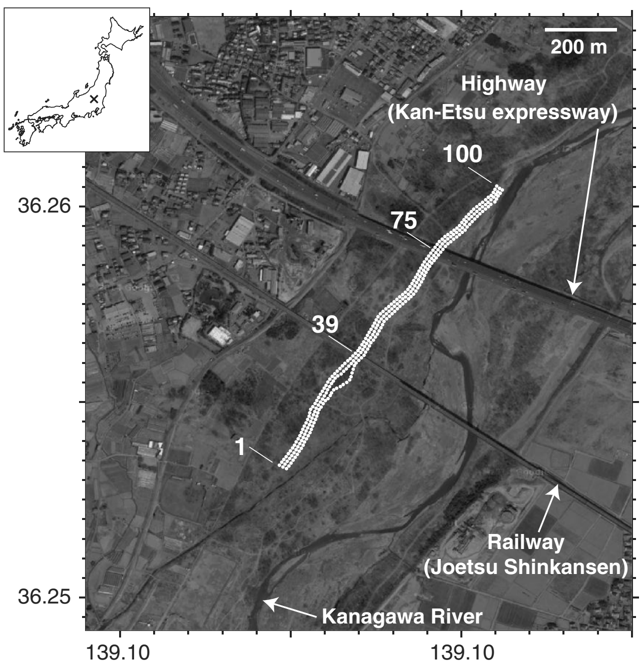

Figure 1. Location of geophones (white dots). The receiver array is along the Kannagawa River and perpendicular to the Joetsu Shinkansen and Kan-Etsu Expressway. The white numbers indicate the receiver numbers (sequential number from the south). The "×" in the inset shows the location of the survey.

Traffic-induced seismic noise

Traffic noise was observed by 300 1C geophones at Gunma, Japan, on 11–15 November 2008 (Figure 1). Two types of data are observed based on the shape of the receiver arrays: three short parallel receiver lines (11–12 November) and one long line (14–15 November). Nakata et al. (2011) use the long line for extracting body and surface waves by coherence-based seismic interferometry and image the subsurface with reflection seismic processing. Here, I use the data recorded by the short lines to study surface waves. The three receiver lines are almost straight and parallel to one another, and each line contains 100 geophones with 10 m spacing (Figure 1). I call these three lines west, central, and east lines, respectively. Traffic noise was almost continuously recorded for approximately 6 h per day during daytime (i.e., total 12 h), and the time-sampling interval was 1 ms. The receivers are single horizontal-component geophones (10 Hz natural frequency), and the azimuth of the component is perpendicular to the direction of the receiver line (i.e., transverse component). Because the distance between each receiver line is also 10 m, every nine receivers are considered to be a square subarray (Figure 2). These subarrays are the size of the array, to which I apply DBF as explained below. Receivers 16–100 on the west line correspond to the receivers 1–85 in Nakata et al. (2011).

The array was deployed along a river (Kannagawa River) and parallel to two small roads (Figure 1). A railway (Joetsu Shinkansen) and highway (Kan-Etsu Expressway), perpendicular to the array, generate variable noise levels among receivers (Figure 3). The railway and highway are elevated for several meters. The noise from the railway is stronger than the one from the

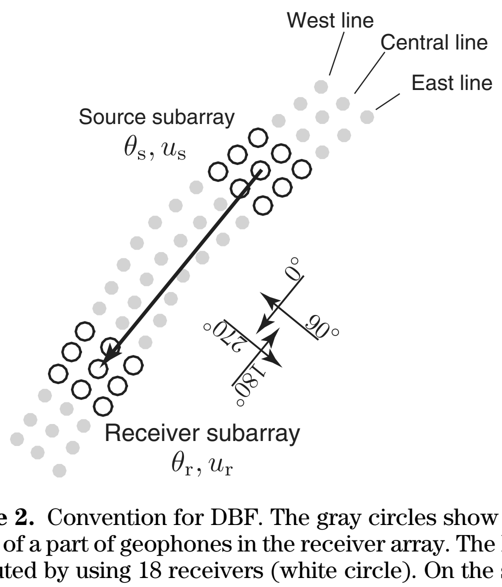

Figure 2. Convention for DBF. The gray circles show the location of a part of geophones in the receiver array. The DBF is computed by using 18 receivers (white circle). On the source and receiver sides, I determine slowness and azimuth for beamforming (θ_s, u_s, θ_r, u_r). The azimuth is defined by the location of central receivers in the source and receiver subarrays (the black arrows). The thick black arrow shows the 0° azimuth.

highway and clearly observed along the entire array, but temporally more sparse than the highway. During the time interval in Figure 3, three trains passed at 2:47, 2:50, and 2:56, respectively. Cars and trucks on the road parallel to the array also generate seismic noise, and in Figure 3a, vehicle noise from the road was observed at 2:45–2:49 around traces 40–100. Based on the power spectra of the observed noise (Figure 3b), the noise generated from the railway is mainly about 10–100 Hz and the highway noise is 0.5–40 Hz (see the frequency ranges in which the gray lines at traces 39 and 75 are greater than the black line). These frequency ranges vary with respect to the type of vehicle, speed, and the condition of the road.

The mechanisms and wave types of traffic noise are not well studied yet, and they probably depend on the condition of each road (types of vehicles, elevated/nonelevated roads, soil around the road, etc.). Based on a 3C study (Behm et al., 2014), Rayleigh and Love waves can be excited from vehicles, and here, I preferentially use Love waves as explained below.

Seismic interferometry and DBF

Similar to Nakata et al. (2011), I use seismic interferometry with crosscoherence (i.e., power-normalized crosscorrelation), which compensates the amplitude balance between receiver pairs and improves the S/N of extracted coherent waves. The crosscoherence between receivers at $\mathbf{x}_\mathrm{s}$ and $\mathbf{x}_\mathrm{r}$ is defined by

$$C(\mathbf{x}_\mathrm{r},\mathbf{x}_\mathrm{s},\omega) = \sum_i \frac{v_i(\mathbf{x}_\mathrm{r},\omega)v_i^*(\mathbf{x}_\mathrm{s},\omega)}{|v_i(\mathbf{x}_\mathrm{r},\omega)||v_i(\mathbf{x}_\mathrm{s},\omega)| + \epsilon\left\langle |v_i(\mathbf{x}_\mathrm{r},\omega)||v_i(\mathbf{x}_\mathrm{s},\omega)|\right\rangle}, \quad (1)$$

where $v_i(\mathbf{x}_\mathrm{s},\omega)$ is the observed wavefield in the frequency domain ω recorded at receiver s at time interval i, ϵ is a regularization parameter ($\epsilon = 0.0001$ here), $\langle \cdots \rangle$ is the ensemble average, and $*$ represents the complex conjugate. After averaging the crosscoherence over long time intervals, $C(\mathbf{x}_\mathrm{r},\mathbf{x}_\mathrm{s},\omega)$ represents the wave propagation from $\mathbf{x}_\mathrm{s}$ to $\mathbf{x}_\mathrm{r}$, where receiver s becomes a virtual source. During the computation of crosscoherence, I remove amplitude information, and hence, I use only the phase information of extracted waves to estimate the S-wave velocity distribution. The length of the time interval is 6 s, and the time windows overlap each other by 80% to stabilize the correlations. First, I average the coherence functions over the entire observations (approximately 12 h) to create C. I compute crosscoherence between all receiver pairs (300×300), although some combinations are not used for further processing (Figure 4a–4c). Strong noise originates from the highway (i.e., strong directionality of traffic noise), so the coherence functions in Figure 4 at traces 75–100 (on the other side of the highway relative to the virtual source) contain waves, which are not physically explained by waves propagating from the virtual source (Chang et al., 2014). Therefore, I do not use the receiver pairs that are across the highway for the dispersion analysis below.

One can use the coherence functions in Figure 4a–4c for surface-wave analyses. However, these coherence functions contain waves that propagate not only parallel to the receiver line but also to other directions because the contribution from the nonstationary phases is not perfectly canceled (Snieder et al., 2008). This contribution of nonstationary phase generates artifacts (i.e., spurious waves). Note that waves propagating parallel to the array are useful for the accurate dispersion analysis. To suppress these nonstationary phases, I apply DBF following Nakata et al. (2016) to each subarray pair (Figure 2). I compute the DBF in the time domain based on a plane-wave projection:

$$B(u_\mathrm{r},\theta_\mathrm{r},u_\mathrm{s},\theta_\mathrm{s},t) = \frac{1}{N_\mathrm{s}N_\mathrm{r}}\sum_{\mathbf{x}_\mathrm{s}}\sum_{\mathbf{x}_\mathrm{r}} C(\mathbf{x}_\mathrm{r},\mathbf{x}_\mathrm{s},t-\tau_\mathrm{s}(\mathbf{x}_\mathrm{s},u_\mathrm{s},\theta_\mathrm{s}) + \tau_\mathrm{r}(\mathbf{x}_\mathrm{r},u_\mathrm{r},\theta_\mathrm{r})), \quad (2)$$

where N is the number of sources and receivers ($N_\mathrm{s} = N_\mathrm{r} = 9$), t is the time, u is the slowness, θ is

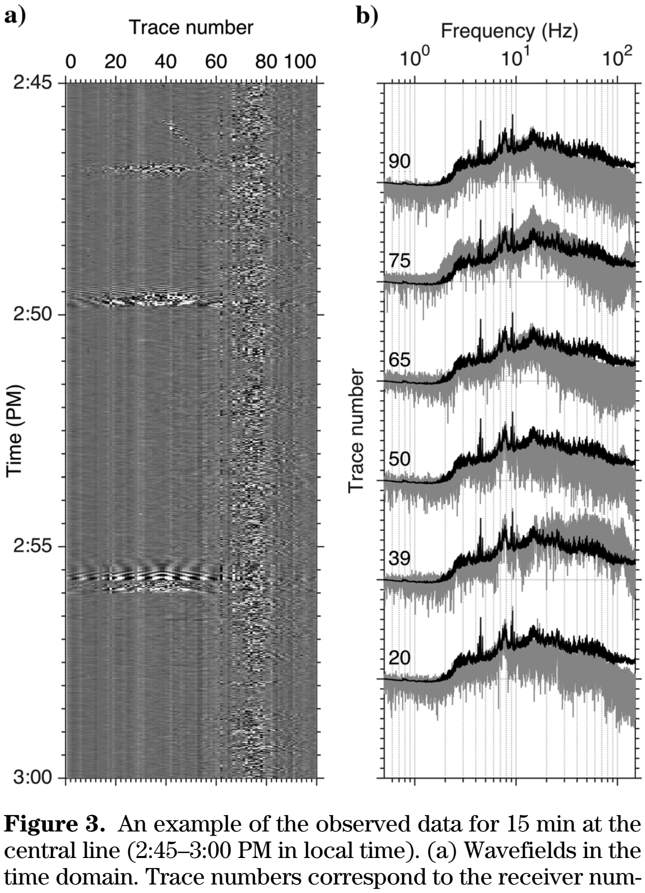

Figure 3. An example of the observed data for 15 min at the central line (2:45–3:00 PM in local time). (a) Wavefields in the time domain. Trace numbers correspond to the receiver number in Figure 1. No band-pass filters are applied. (b) Power spectra in the frequency domain. The numbers indicate the trace number. The gray lines show the spectra at each trace, and the black lines show the average spectra over all traces for a reference.

the azimuth, and τ is the time lag for beamforming. The nine geophones create a square-shaped source/receiver subarray, and the central receivers at each subarray define the azimuth θ (Figure 2). The time lag τ is a relative time delay from the central receiver (x^c, y^c):

$$\tau_s = u_s(x_s - x_s^c)\cos\theta_s + u_s(y_s - y_s^c)\sin\theta_s, \quad (3)$$

for τ_s and similar expression for τ_r. In equation 3, $x - x^c$ and $y - y^c$ show the distances from the central receiver in the x- and y-directions, respectively (Figure 2). To extract the wave propagation between two points, B uses 81 coherence functions and averages them based on equations 2 and 3. Therefore, I can control the azimuth and slowness of the retrieved waves to preferentially use the contribution from the stationary phase.

Figure 4d–4g shows the virtual shot gathers after DBF in four different azimuths. At each receiver pair in the central line, I use the surrounding eight receivers to make subarrays and apply DBF (Figure 2). Due to the dominant direction of the strong traffic noise, the 0° DBF function shows the clearest wave propagation (Figure 4d). The extracted waves in Figure 4d and 4f mostly contain Love waves because of the following reasons: (1) After DBF, the waves propagate perpendicular to the receiver component, and (2) the extracted waves are dispersive. The group velocity of the dominant Love wave is approximately 430 m/s that propagates from the virtual source to the end of the array (trace 1). Ambient noise in the 180° direction also has some contribution for constructing the surface-wave signals (i.e., traces 65–80 in the positive time in Figure 4f). These signals are mainly related to the seismic energy generated by trains on the railroad around receiver 39. Cars along the small road parallel to the array at the northwest of the receivers (Figure 1) also generate some coherent waves, and hence, the coherent arrivals in Figure 4g show more energy than Figure 4e. Because the waves propagate perpendicular to the receiver line and the distance from the array to the small road is short around receivers 40–70, the extracted wavefields have larger apparent slownesses in Figure 4g.

Because the subarray is relatively small, the ability to isolate the target waves is limited (as shown by Nakata et al. [2016], the maximum improvement of S/N is a factor of nine with this subarray); therefore, wavefields in Figure 4e–4g provide noticeable arrivals incident from 0°. Importantly, by using DBF, I enhance the coherency of the wave propagation and reduce incoherent random

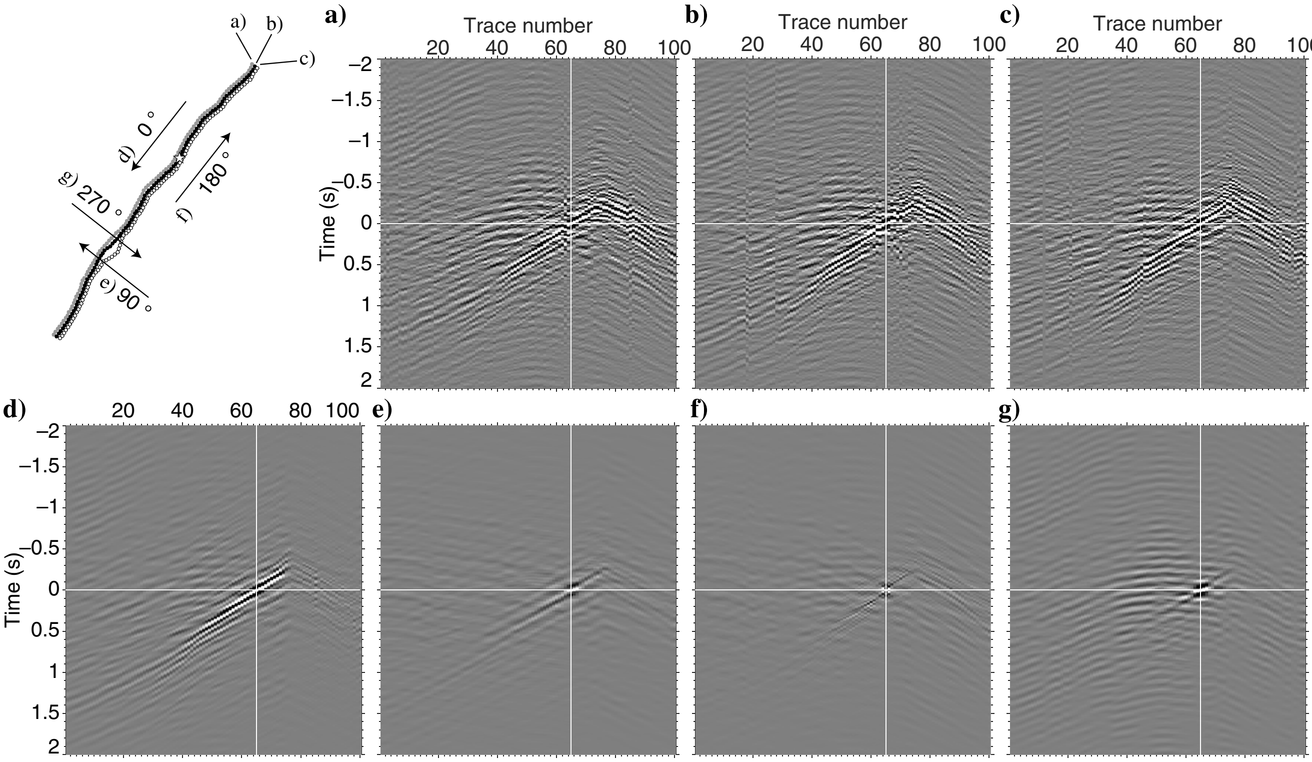

Figure 4. Example of virtual shot gathers. The top-left map shows the receiver location with explanation of each panel. The white star shows the location of the virtual source (receiver 65). Panels (a–c) show virtual shot gathers at each line and panels (d–g) show virtual shot gathers after DBF. The slowness range of DBF is from 0.7 to 5.0 s/km. The azimuth of DBF is defined by the top-left map, and I average wavefields over $\pm 20^{\circ}$ from the azimuth in the map (i.e., 160°–200°for panel [f]). In each panel, the vertical white line shows the trace of the virtual source and the horizontal line the origin time. The frequency range is from 7 to 30 Hz. The relative amplitudes are preserved between panels.

noise. Considering the array shape and the stationary phase assumption, I use 0° and 180° wavefields at 100 subarrays for further dispersion analysis.

The power spectra show the improvement of the S/N for extracted Love waves (Figure 5a), and Figure 5b shows the coherent spectra along receivers. The abrupt change of the spectra at trace 75 in Figure 5b is caused by the strong noise directionality related to the highway.

The DBF is also helpful for extracting very high-frequency waves (Figure 6). These waves are very hard to identify without using DBF (Figure 6a). The waves at 50–100 Hz propagate approximately 20 m before dissipating into the background noise level. Based on the dispersion analysis below, I consider that these high-frequency waves are either higher mode Love waves or S-waves because the wave velocity is too high for fundamental-mode Love waves at this area.

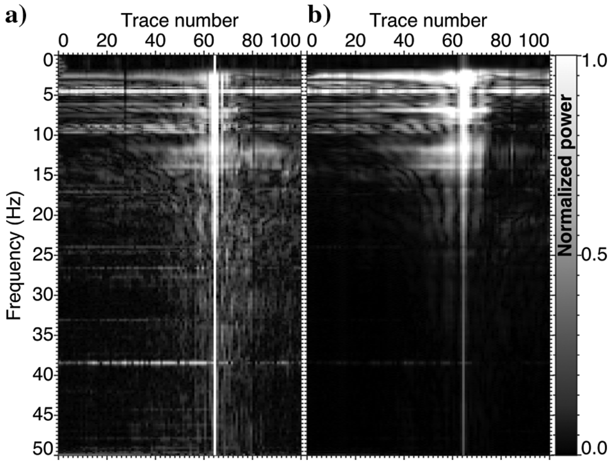

Figure 5. Power spectra of the virtual shot gather: (a) central line (spectra of Figure 4b) and (b) 0° DBF (spectra of Figure 4d). The power spectra are normalized in each panel.

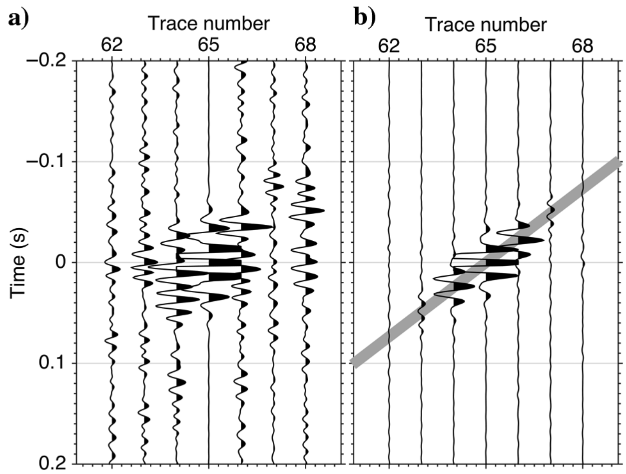

Figure 6. Virtual shot gathers in the frequency range from 50 to 100 Hz: (a) central line and (b) 0° DBF. The gray line shows the arrival time of the wave with the velocity of 400 m/s.

CMP-based surface-wave analysis

Estimation of 2D velocity model

I analyze dispersion curves of the extracted surface waves at each CMP gather after seismic interferometry and DBF. The CMP-based dispersion analysis increases the lateral resolution. Hayashi and Suzuki (2004) and Ikeda et al. (2013) apply this dispersion analysis to active-source surface-wave data and compute crosscorrelations between all receiver pairs to find the phase differences (named CMP crosscorrelation or CMPCC). For the virtual shot gathers used (Figure 4), I consider that CMP gathers of correlation functions are equivalent to CMPCC, and hence, I do not crosscorrelate wavefields again between receivers for each virtual source. Because the array is almost along a straight line, I take the CMP trace spacing to be 5 m along a line (half of the receiver spacing).

Ikeda et al. (2013) mention that the long-offset receiver pairs decrease the lateral resolution. There-

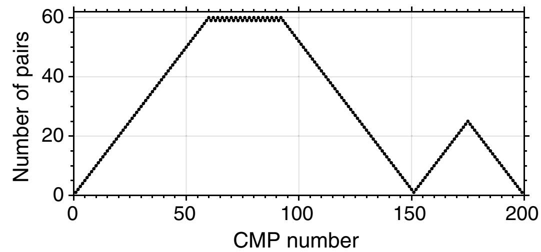

Figure 7. Number of receiver pairs at each CMP. The CMP spacing is the half of the receiver spacing (i.e., 5 m).

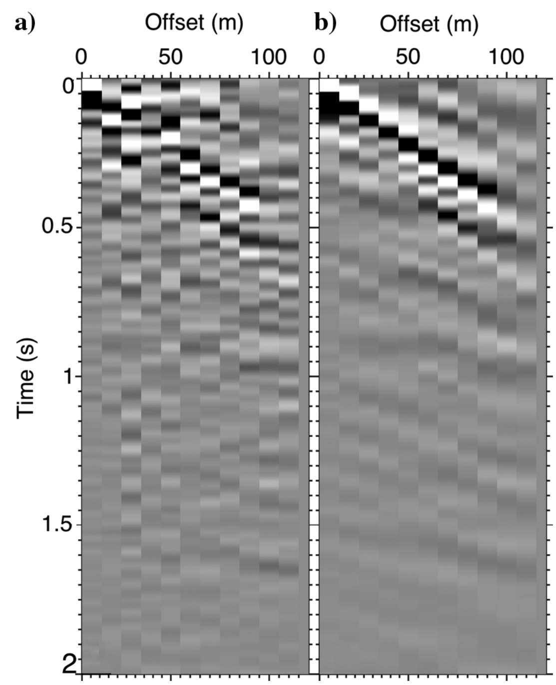

Figure 8. CMP gathers at CMP 130 (at receiver number 65) (a) at the central line and (b) with DBF. The frequency range is 4–20 Hz.

fore, I set the maximum offset at 300 m after testing different offsets (see Figure 4d–4g to understand the S/N of Love waves against the offset). By considering two directions of the wave propagation (0° and 180°), the maximum number of receiver pairs at each CMP is 60 (Figure 7). For making CMP gathers, I do not use the receiver pairs that contain the highway (at CMP 150) inside the receivers because of the strong nonphysical waves as explained above. This is an important step for this data set to accurately estimate dispersion curves by avoiding the pseudowaves as very fast traveling waves. At each offset in one CMP gather, two wavefields exist except at zero offset (i.e., receiver A → B and B → A), and I average wavefields propagating at 0° and 180° (i.e., 0° for A → B and 180° for B → A). Hence, the causal and acausal waves are symmetrically located about the origin at $t = 0$ s. Note that the causal waves propagating at 0° A → B and the acausal waves 0° B → A are identical.

Figure 8 shows the ability of DBF to improve the coherency of the extracted wavefields in the CMP gather at CMP 130. The maximum offset of this CMP gather is 110 m, which corresponds to the distance from the CMP to the highway. Although the fundamental Love waves at velocities of 250–300 m/s are retrieved by crosscorrelations at each line (Figure 8a), the coherency of the waves is dramatically increased after DBF (Figure 8b). Even later phases (i.e., after 0.5 s) are extracted coherently. These waves are useful for, e.g., estimating small stiffness changes with time-lapse surveys (Snieder et al., 2002). The S/N of the phase velocity-frequency spectrogram is also increased after DBF (compare Figure 9a and 9b). In addition to the clear fundamental-mode Love waves, by using DBF, I can reconstruct higher modes, identified by the shape of the bright spots in the spectrogram. Here, I focus on the fundamental mode and pick phase velocities at each frequency to estimate dispersion curves.

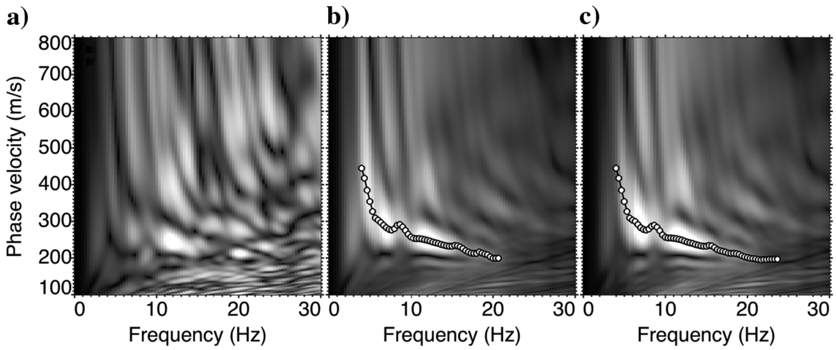

Figure 9. Phase velocity-frequency spectrogram at CMP 130 (at receiver number 65) (a) at the central line and (b and c) after DBF. Panels (a and b) are obtained from Figure 8a and 8b, respectively. The picked dispersion curves at each frequency are indicated by the white circles. The maximum offsets are (a and b) 300 m and (c) based on Ikeda et al. (2013).

To further improve the lateral resolution of the surface-wave analysis, I use the window-controlled CMP analysis (Ikeda et al., 2013). Because the sensitivity of the waves to subsurface structure is related to their wavelengths, the size of the spatial window depends on the wavelengths. Following Ikeda et al. (2013), at each frequency, I limit the maximum offset for CMP gathers based on the wavelength, which is computed by the dispersion curves in Figure 9b (maximum offset of 300 m). Figure 9c shows the spectrogram after offset windowing ($\alpha = 0.5$ in equation 7 in Ikeda et al., 2013). The window-controlled CMP improves the S/N of the spectrogram, especially for high frequencies. To retain a sufficient number of traces for the dispersion analysis while increasing the lateral resolution, I set the minimum and maximum offsets as 30 and 300 m, respectively. One can iteratively update the wavelengths using the dispersion curve in Figure 9c, but the results have almost no further change in this data set.

I estimate phase velocities at each CMP location after offset windowing (Figure 10a). For accurate estimation of the dispersion curves, I use only CMP gathers that contain more than five traces. Around the horizontal distances 500–900 m, I can also accurately pick the high-frequency dispersion curves, which might be caused by the location of the traffic-noise sources and/or reverberations in the subsurface structure. At each CMP, I invert the dispersion curves to estimate the S-wave velocities by assuming the 1D structure based on Mokhtar et al. (1988) and Herrmann (2013). Because I use Love waves, the surface waves are not sensitive to P-velocity distribution. The initial model

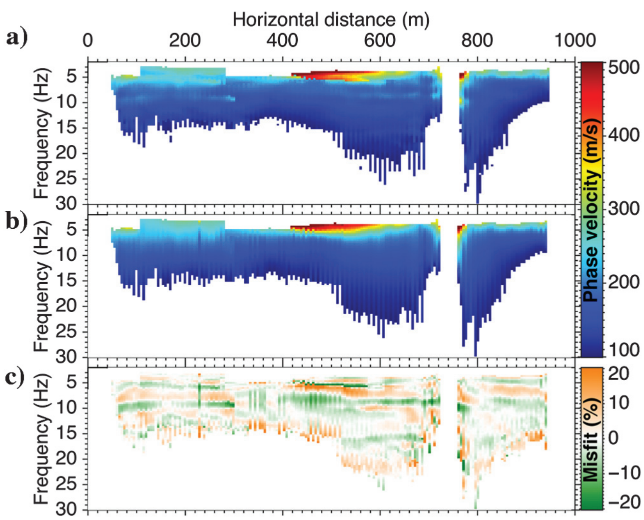

Figure 10. (a) Observed dispersion curves for the fundamental-mode Love waves at each CMP location. The maximum offset is based on Ikeda et al. (2013). (b) Inverted dispersion curves from panel (a). (c) Misfits between the dispersion curves shown in panels (a and b).

for the inversion is the 1D S-velocity model obtained by Nakata et al. (2011). Although I do not set the number of layers for the inversion, I use a damping parameter to obtain a smooth depth variation in velocities in depth (Behm et al., 2016). Based on the wavelength of the Love waves (Socco et al., 2010), the depth sensitivity is down to 60–100 m and I invert the velocities down to 80 m. Figure 10b shows the dispersion curves after inversion. To create the 2D velocity model, I compute the inversion at all CMPs and apply a three-trace lateral smoothing (Figure 11a).

Discussion of inverted near-surface S-wave velocity model

Based on the misfits of the dispersion curves between observation and inversion (Figure 10c), the observed curves are explained well by the inverted velocity model. Because the dispersion curves are smoothed during the inversion due to the damping parameter, larger misfit values are observed at narrow frequency bands (e.g., approximately 10 Hz). However, this smoothing is necessary to stabilize the inversion, and I set the damping parameter as small as possible for fast convergence.

The horizontal distances of 350–950 m in Figure 11 roughly correspond to CMPs 20–80 in Figure 6 in Nakata et al. (2011). The velocity model in Figure 11a shows similar features in the reflection images. For example, two main features of the velocity model are shown in the reflected images (especially Figure 6d): an abrupt velocity changes at 460 m and a down-dip from 520 to 900 m. Because Nakata et al. (2011) use a different velocity model for the images, and the frequency ranges used are different, I do not attempt to compare the velocity model in more detail with the reflection image. The thick low-velocity zone at 130–280 m might be related to the damp ground in this area, where even unpaved roads do not exist around receivers 0–200 m (see Figure 1). According to the geologic map issued by the Geological Survey in Japan, the surface sediments in this area are composed of river-bed deposits (gravel, sand, and mud), but no spatial variations are shown.

For engineering/environmental purposes or for static correction of active-source imaging, 12 h of observation of ambient noise is sometimes too long to implement. Thus, I test the quality of the velocity model using only 1 h of data (Figure 11b). Except for the length of the input data, I follow the same procedure used for Figure 11a. To examine the stability of the hourly velocity models, I also compute the perturbation of the estimated velocities as standard deviation of hourly velocities divided by the velocities shown in Figure 11a (Figure 11c). I use 12 velocity models (i.e., 12 h of data) for estimating the standard deviation. The red-purple color in Figure 11c indicates locations where the estimation varies over hours. The velocity variations are mostly within 3%–4%, and the highest value is approximately 10%. The 4% perturbations are considered as accurate enough for many engineering purposes and show potential to obtain subsurface information in the short-time data acquisition. Therefore, I conclude

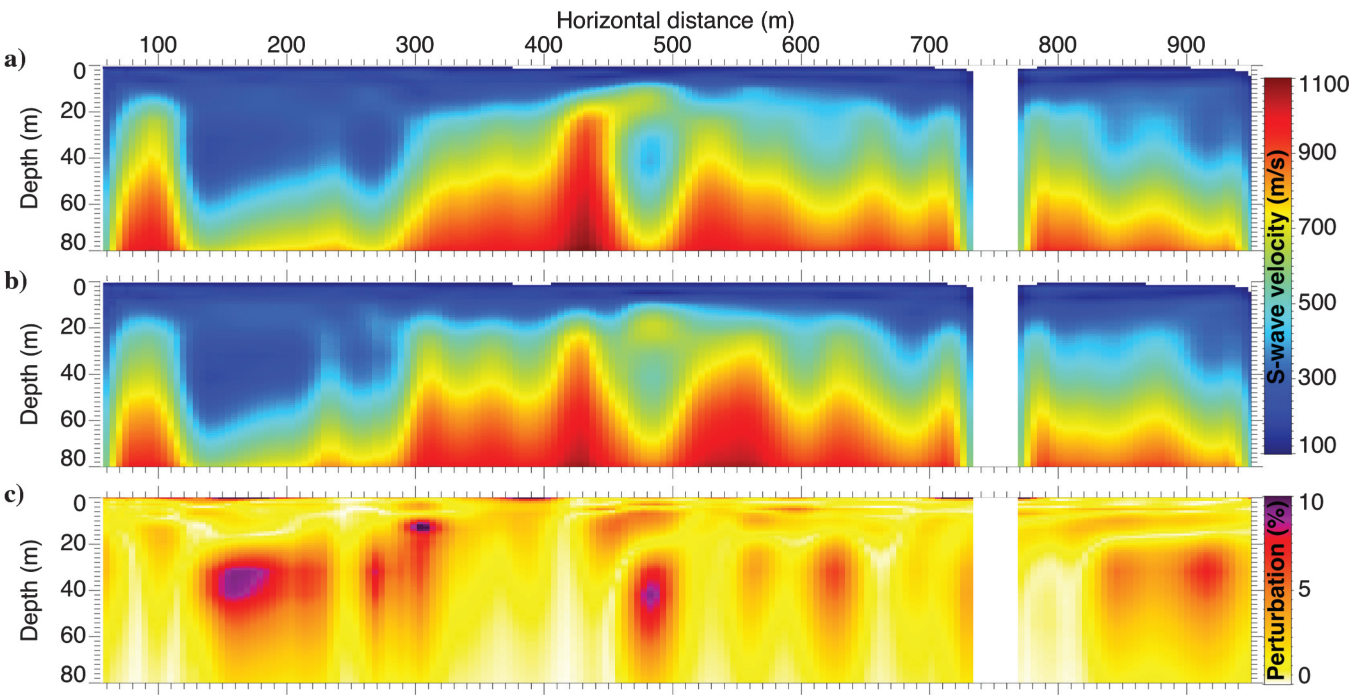

Figure 11. (a) Inverted S-wave velocities from the dispersion curves shown in Figure 10. (b) Inverted S-wave velocities using only 1 h traffic noise data. (c) Perturbations of S-wave velocities over each hour. The perturbations are given as the standard deviation of hourly velocities divided by the velocities shown in panel (a).

that even for 1 h data, I obtain a useful estimate of the velocity distribution. The minimum time length of observation is dependent on the time-varying traffic noise, but the result in Figure 11b is encouraging for many applications.

Conclusions

I apply seismic interferometry with DBF to traffic noise for estimating the 2D near-surface S-velocity distribution. The DBF is useful for satisfying the stationary phase assumption in ambient noise seismology to extract surface waves with high S/N. For horizontal component geophones with particle motion perpendicular to the line direction, the extracted surface waves are mainly Love waves. When other components of geophones exist, one could use the same technique as shown in this study for Rayleigh waves. To enhance lateral resolution of surface waves, I use window-controlled CMP for the dispersion analysis. This analysis limits the maximum offset of receiver pairs based on the wavelengths, which is important for accurately estimating local dispersion curves. The 2D velocity models show the detailed S-velocity structure down to 80 m. Even with 1 h of ambient-noise data, I can estimate a similar velocity model. This demonstrates that we need a very short time of observation to estimate the near-surface velocities, which is useful for geophysical engineering and static corrections. Time-lapse monitoring with very short-time intervals is another interesting application.

Acknowledgments

I am grateful to Z. Spica at Stanford University for his professional comments, and K. Onishi at Akita University, T. Kurahashi at Public Works Research Institute, and T. Aizawa at Suncoh Consultants for the acquisition of the seismic data.

References

Aki, K., 1957, Space and time spectra of stationary stochastic waves, with special reference to microtremors: Bulletin of the Earthquake Research Institute, **35**, 415–456.

Behm, M., G. M. Leahy, and R. Snieder, 2014, Retrieval of local surface wave velocities from traffic noise — An example from the La Barge basin (Wyoming): Geophysical Prospecting, **62**, 223–243, doi: 10.1111/1365-2478.12080.

Behm, M., N. Nakata, and G. Bokelmann, 2016, Regional ambient noise tomography in the Eastern Alps of Europe: Pure and Applied Geophysics, 1–28, doi: 10.1007/s00024-016-1314-z.

Boué, P., P. Roux, M. Campillo, and X. Briand, 2014, Phase velocity tomography of surface waves using ambient noise cross correlation and array processing: Journal of Geophysical Research, **119**, 519–529, doi: 10.1002/2013JB010446.

Brenguier, F., N. M. Shapiro, M. Campillo, A. Nercessian, and V. Ferrazzini, 2007, 3-D surface wave tomography of the Piton de la Fournaise volcano using seismic noise correlations: Geophysical Research Letters, **34**, L02305, doi: 10.1029/2006GL028586.

Chang, J. P., N. Nakata, R. G. Clapp, and B. Biondi, 2014, High-frequency surface and body waves from ambient noise cross-correlations at Long Beach, CA: 84th Annual International Meeting, SEG, Expanded Abstracts, 2235–2239.

Claerbout, J. F., 1968, Synthesis of a layered medium from its acoustic transmission response: Geophysics, **33**, 264–269, doi: 10.1190/1.1439927.

Ekström, G., 2001, Time domain analysis of Earth's long-period background seismic radiation: Journal of Geophysical Research, **106**, 26483–26493, doi: 10.1029/2000JB000086.

Gabriels, P., R. Snieder, and G. Nolet, 1987, In situ measurements of shear-wave velocity in sediments with higher-mode Rayleigh waves: Geophysical Prospecting, **35**, 187–196, doi: 10.1111/j.1365-2478.1987.tb00812.x.

Hayashi, K., and H. Suzuki, 2004, CMP cross-correlation analysis of multi-channel surface-wave data: Exploration Geophysics, **35**, 7–13, doi: 10.1071/EG04007.

Herrmann, R. B., 2013, Computer programs in seismology: An evolving tool for instruction and research: Seismological Research Letters, **84**, 1081–1088, doi: 10.1785/0220110096.

Ikeda, T., T. Tsuji, and T. Matsuoka, 2013, Window-controlled CMP crosscorrelation analysis for surface waves in laterally heterogeneous media: Geophysics, **78**, no. 6, EN95–EN105, doi: 10.1190/geo2013-0010.1.

Lin, F.-C., D. Li, R. W. Clayton, and D. Hollis, 2013, High-resolution 3D shallow crustal structure in Long Beach, California: Application of ambient noise tomography on a dense seismic array: Geophysics, **78**, no. 4, Q45–Q56, doi: 10.1190/geo2012-0453.1.

Lobkis, O. I., and R. L. Weaver, 2001, On the emergence of the Green's function in the correlations of a diffuse field: Journal of the Acoustical Society America, **110**, 3011–3017, doi: 10.1121/1.1417528.

Mokhtar, T. A., R. B. Herrmann, and D. R. Russell, 1988, Seismic velocity and Q model for the shallow structure of the Arabian shield from short-period Rayleigh waves: Geophysics, **53**, 1379–1387, doi: 10.1190/1.1442417.

Mordret, A., M. Landès, N. M. Shapiro, C. Singh, P. Roux, and O. I. Barkved, 2013, Near-surface study at the Valhall oil field from ambient noise surface wave tomography: Geophysical Journal International, **193**, 1627–1643, doi: 10.1093/gji/ggt061.

Nakata, N., P. Boué, F. Brenguier, P. Roux, V. Ferrazzini, and M. Campillo, 2016, Body- and surface-wave reconstruction from seismic-noise correlations between arrays at Piton de la Fournaise volcano: Geophysical Research Letters, **43**, 1047–1054, doi: 10.1002/2015GL066997.

Nakata, N., J. P. Chang, J. F. Lawrence, and P. Boué, 2015, Body-wave extraction and tomography at Long Beach, California, with ambient-noise interferometry: Journal of Geophysical Research, **120**, 1159–1173, doi: 10.1002/2015JB011870.

Nakata, N., R. Snieder, T. Tsuji, K. Larner, and T. Matsuoka, 2011, Shear-wave imaging from traffic noise using seismic interferometry by cross-coherence: Geophysics, **76**, no. 6, SA97–SA106, doi: 10.1190/geo2010-0188.1.

Nishida, K., J.-P. Montagner, and H. Kawakatsu, 2009, Global surface wave tomography using seismic hum: Science, **326**, 112–112, doi: 10.1126/science.1176389.

Park, C. B., R. D. Miller, and J. Xia, 1999, Multichannel analysis of surface waves: Geophysics, **64**, 800–808, doi: 10.1190/1.1444590.

Park, C. B., R. D. Miller, J. Xia, and J. Ivanov, 2007, Multichannel analysis of surface wave (MASW) — Active and passive methods: The Leading Edge, **26**, 60–64, doi: 10.1190/1.2431832.

Peterson, J., 1993, Observations and modeling of seismic background noise: U.S. Geological Survey, Technical Report 93–322.

Rost, S., and C. Thomas, 2002, Array seismology: Methods and applications: Reviews of Geophysics, **40**, 1008, doi: 10.1029/2000RG000100.

Roux, P., B. D. Cornuelle, W. A. Kuperman, and W. S. Hodgkiss, 2008, The structure of raylike arrivals in a shallow-water waveguide: Journal of the Acoustical Society America, **124**, 3430–3439, doi: 10.1121/1.2996330.

Shapiro, N. M., M. Campillo, L. Stehly, and M. H. Ritzwoller, 2005, High-resolution surface-wave tomography from ambient seismic noise: Science, **307**, 1615–1618, doi: 10.1126/science.1108339.

Snieder, R., 2004, Extracting the Green's function from the correlation of coda waves: A derivation based on stationary phase: Physical Review E, **69**, 046610, doi: 10.1103/PhysRevE.69.046610.

Snieder, R., A. Grêt, H. Douma, and J. Scales, 2002, Coda wave interferometry for estimating nonlinear behavior in seismic velocity: Science, **295**, 2253–2255, doi: 10.1126/science.1070015.

Snieder, R., K. van Wijk, M. Haney, and R. Calvert, 2008, Cancellation of spurious arrivals in Green's function extracting and the generalized optical theorem: Physical Review E, **78**, 036606, doi: 10.1103/PhysRevE.78.036606.

Socco, L. V., S. Foti, and D. Boiero, 2010, Surface-wave analysis for building near-surface velocity— Established approaches and new perspectives: Geophysics, **75**, no. 5, 75A83–75A102,doi: 10.1190/1.3479491.

Wapenaar, K., 2004, Retrieving the elastodynamic Green's function of an arbitrary inhomogeneous medium by cross correlation: Physical Review Letters, **93**, 254301, doi: 10.1103/PhysRevLett.93.254301.

Young, M. K., N. Rawlinson, P. Arroucau, A. M. Reading, and H. Tkalčić, 2011, High-frequency ambient noise tomography of southeast Australia: New constraints on Tasmania's tectonic past: Geophysical Research Letters, **38**, L13313, doi: 10.1029/2011GL047971.

Nori Nakata received a B.S. (2008) and an M.S. (2010) in engineering from Kyoto University, and a Ph.D. (2013) at Colorado School of Mines. He joined the Department of Geophysics at Stanford University in September 2013 as the George Thompson Postdoctoral Research Fellow. His expertise is across signal processing and physics-based wave phenomena. His research interests include crustal/global seismology, exploration geophysics, volcanism, and civil engineering using passive and active seismic data to gain better understanding of structures and seismic sources with 3D/4D imaging.